

# Electrical detection of high-order optical orbital angular momentum

Guanyu Zhang<sup>1</sup>, Xianghan Meng<sup>1</sup>, Zini Cao<sup>1</sup>, Hai Lin<sup>2</sup>, Shuxin Huang<sup>1</sup>, Minghao Deng<sup>1</sup>, Jiaqi Li<sup>1</sup>,  
Qihuang Gong<sup>1, 3, 4</sup>, and Guowei Lyu<sup>1, 3, 4\*</sup>

<sup>1</sup> *State Key Laboratory for Mesoscopic Physics, Collaborative Innovation Center of Quantum Matter, Frontiers Science Center for Nano-Optoelectronics, School of Physics, Peking University, Beijing 100871, China*

<sup>2</sup> *School of energy and physics, Huizhou University, Huizhou, Guangdong 516007, China*

<sup>3</sup> *Collaborative Innovation Center of Extreme Optics, Shanxi University, Taiyuan, Shanxi 030006, China*

<sup>4</sup> *Peking University Yangtze Delta Institute of Optoelectronics, Nantong, Jiangsu 226010, China*

\* Corresponding author: [guowei.lyu@pku.edu.cn](mailto:guowei.lyu@pku.edu.cn)

## Abstract

The orbital angular momentum (OAM) of light provides an infinite orthogonal basis for information capacity in optical communications and high-dimensional quantum processing. However, harnessing this potential in integrated systems is hindered by the lack of compact devices capable of direct electrical readout of high-order OAM modes. Here, we report an on-chip silicon-based integrated photodetector that directly converts optical OAM into distinguishable electrical signals without bulky interferometric or imaging optics. By leveraging a momentum-matched plasmonic coupling mechanism, the device maps vortex beams onto surface plasmon polaritons (SPPs) with OAM-dependent splitting angles, thereby generating photocurrents that uniquely encode the topological charge. The incorporation of a surface dielectric lens and a split-electrode architecture further enhances mode resolution and enables chirality discrimination. The device demonstrates a wide topological charge detection range from  $m = -9$  to 9 and achieves a record-high average OAM responsivity of  $226 \text{ nA} \cdot \text{W}^{-1}$ . By bridging the gap between vortex beams and electronic readout on a scalable platform, this work paves the way for on-chip OAM direct detection for next-generation high-capacity optical networks.

## Introduction

Optical orbital angular momentum (OAM) in vortex beams, as a distinct degree of freedom of light, has attracted growing attention for its wide-ranging applications in optomechanical manipulation<sup>1,2</sup>, super-resolution imaging<sup>3</sup>, sensing<sup>4,5</sup>, and quantum information processing<sup>6</sup>. OAM theoretically supports an infinite set of mutually orthogonal optical modes, offering great potential to enhance the capacity and security of both classical<sup>7,8</sup> and quantum<sup>9</sup> optical communications. Consequently, the development of multi-mode, high-speed OAM detection technologies is of critical importance for advancing vortex-beam-based communication systems.

Conventional OAM detection methods rely on light interference<sup>10</sup> and diffraction<sup>11</sup>, where the OAM state is determined by analyzing interference fringes or diffraction patterns. Alternatively, spatial light modulators combined with lenses can convert OAM states into distinct spatial positions for identification<sup>12</sup>. However, these approaches typically require bulky optical setups, limiting their compatibility with on-chip integration. With the advent of nano-optics, metasurfaces have emerged as compact alternatives to spatial light modulators<sup>13,14</sup>, yet they still depend on complex imaging systems. Surface plasmon polaritons (SPPs) offer a promising route toward miniaturized OAM detection. When excited by vortex beams, SPPs inherit angular momentum determined by both the incident light and the excitation geometry<sup>15</sup>. Properly engineered nanostructures, such as annular gratings<sup>16,17</sup> or apertures<sup>18</sup>, can separately focus or selectively transmit SPPs excited by different OAM states, thereby enabling OAM discrimination. Nonetheless, most of these techniques continue to rely on far-field imaging<sup>19</sup> or even near-field probing<sup>20</sup> systems. Hence, developing integrated OAM photodetectors with multi-mode detection

capability and direct electrical readout remains a critical challenge for next-generation on-chip compact high-capacity communication systems.

Although the multiplexing and discrimination of vortex beams have been extensively explored, direct electrical detection of light OAM remains scarce. Reported devices can be broadly classified into two categories: SPP-based and orbital photogalvanic effect (OPGE)-based photodetectors. For example, in SPP-based schemes, gratings are designed as holographic strips that can be excited by specific OAM modes. When coupled with conventional photodetectors, these structures enable selective detection of a single vortex beam<sup>21</sup>. To achieve multi-mode detection, a PdSe<sub>2</sub>-based photothermal detector acting as a spot position sensor has been integrated with a spin-Hall plasmonic grating<sup>22</sup>. The grating directs vortex beams with different angular momenta into spatially separated SPP foci, which are subsequently converted into electrical signals by the PdSe<sub>2</sub> detector, achieving OAM detection up to a OAM order of  $m = 4$ .

The OPGE, a second-order photoelectric effect driven by the helical phase gradient of light, generates photocurrents proportional to the beam's OAM order. This mechanism, which provides a direct link between OAM and photocurrent, was first observed in low-symmetry two-dimensional WTe<sub>2</sub><sup>23</sup>, and later reported in TaIrTe<sub>4</sub><sup>24</sup> and multilayer graphene<sup>25,26</sup>. However, extracting the OPGE signal requires differential measurements under left- and right-circularly polarized illumination, making the method noise-sensitive and unsuitable for high-speed communication. To date, no on-chip OAM photodetector has demonstrated electrical detection of vortex beams beyond OAM orders  $m = 4$ . Moreover, the majority of existing devices depend on scarce two-dimensional materials, for which large-scale fabrication technologies are still under development.

In this work, we present a silicon-based photodetector capable of directly converting optical OAM into electrical signals. With a compact grating architecture, the device achieves a maximum detectable topological charge of  $|m| = 9$ , which significantly expands the capacity of on-chip OAM detection. The grating couples vortex beams possessing different angular momenta into SPP modes that propagate in distinct directions, and experience OAM-dependent losses, which are subsequently transferred to the Schottky junction, generating photocurrents that encode the beam's topological charge. Incorporating a surface dielectric lens further enhances the discrimination between adjacent OAM states, facilitating precise determination of the topological charge. Moreover, the handedness of the vortex beam can be determined by comparing the relative intensities of the SPP branches. The device achieves an average OAM responsivity of  $226 \text{ nA} \cdot \text{W}^{-1}$ , outperforming all previously reported studies. With a noise-equivalent OAM resolution down to  $0.05 \text{ Hz}^{-1/2}$ , it lays a solid foundation for robust on-chip OAM detection and presents a promising pathway toward next-generation high-capacity optical technologies, including sensing, communication, and quantum information processing.

## Results

### On-chip OAM photodetector as a proof of concept

The orbital angular momentum of light arises from the helical phase front that winds around the beam axis and is characterized by the quantized OAM order, i.e., topological charge  $m$ . It can be expressed as the phase gradient integral looping around the beam's central singularity,  $m = \frac{1}{2\pi} \oint_C \varphi(\mathbf{r}) d\mathbf{r}$ , where  $\varphi$  is the optical phase, and  $\mathbf{r}$  is the position vector. For a vortex beam, the helical phase front implies that the local wave vector is tilted with respect to the propagation

direction, yielding an in-plane component,  $k_{OAM} = k \cdot \frac{n_{\parallel}}{|\mathbf{n}|}$ , where  $k$  is the magnitude of the free-space wave vector,  $\mathbf{n}$  is the unit normal to the wavefront, and  $n_{\parallel}$  is its projection parallel to the detector plane. As  $m$  increases, the phase winds more rapidly within one wavelength, leading to stronger front twisting and consequently a larger in-plane wave vector (see Supplementary Note 1 for details).

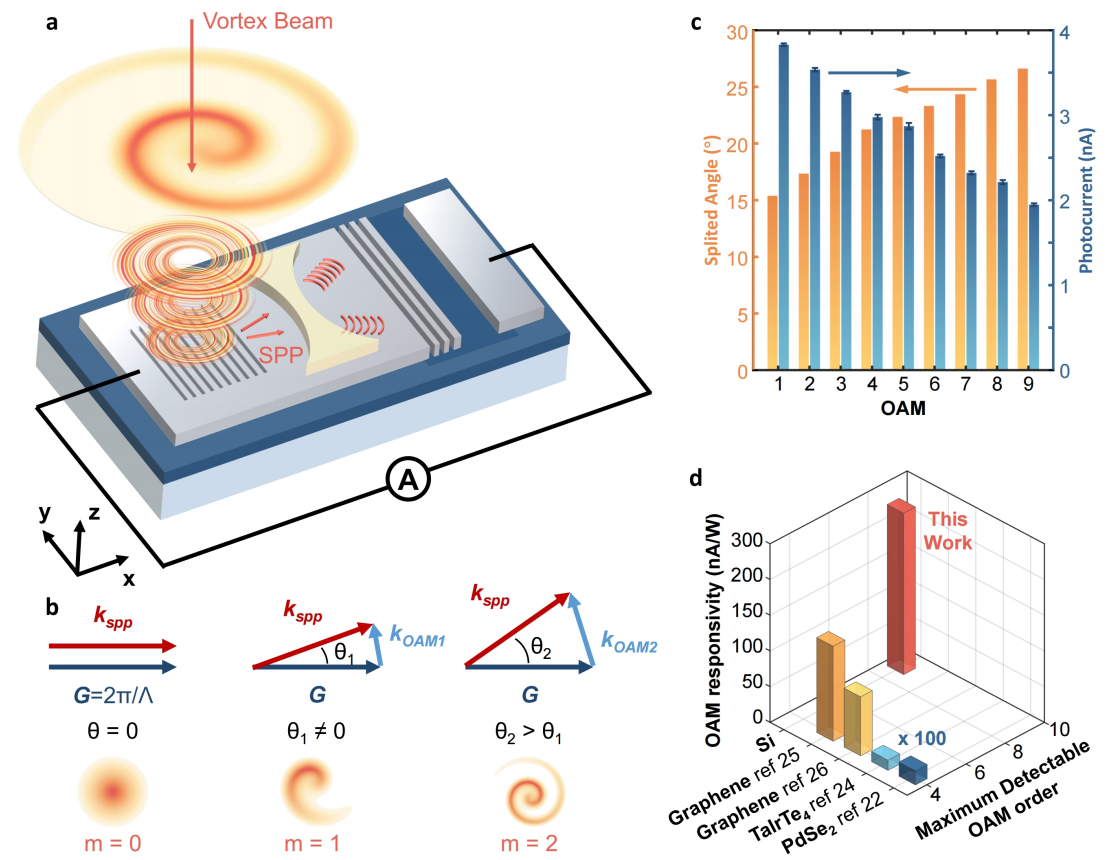


**Fig. 1 Device architecture and operational principle of the vortex beam photodetector. a.** Schematic illustration of the OAM photodetection methods. The incident vortex beam couples to specific SPPs via the plasmonic grating, generating an encoded photocurrent response. **b.** Vector diagrams representing the momentum matching condition for vortex beams with  $m = 0, 1$ , and  $2$ . The SPP propagation angle increases with the OAM order. **c.** Simulated splitting angles (orange) and measured photocurrents (blue) for incident vortex beams with OAM orders  $m$  ranging from 1 to 9. **d.** 3D bar chart comparing OAM responsivity (nA/W) for various materials. The x-axis is Maximum Detectable OAM order, the y-axis is OAM responsivity (nA/W), and the z-axis is material. The chart includes data for Si, Graphene (ref 25, 26), Ta<sub>2</sub>Te<sub>4</sub> (ref 24), and PdSe<sub>2</sub> (ref 22). A red bar labeled "This Work" is shown for the device presented in the figure, with a value of approximately 300 nA/W at a maximum detectable OAM order of 8. A scale factor of "x 100" is indicated for the y-axis.

to 9. Error bars indicate standard deviations. **d.** Comparison of OAM responsivity and maximum detectable OAM order against state-of-the-art direct OAM photodetectors.

Fig. 1a schematically illustrates the concept of the on-chip OAM photodetector, which employs a planar silicon-based architecture incorporating input and output coupling gratings on one side of the electrode. Both gratings are one-dimensional linear structures, and a dielectric lens is integrated between them to expand the detectable OAM range. During measurement, a slightly focused vortex beam is normally incident at the center of the input grating, exciting SPPs that satisfy the momentum-matching condition (Fig. 1b),  $\mathbf{k}_{\text{spp}} = \mathbf{G} + \mathbf{k}_{\text{OAM}}$ , where  $\mathbf{G}$  is the reciprocal lattice vector of the grating and  $\mathbf{k}_{\text{spp}}$  is the plasmon wave vector. In the experiments, four positions on the vortex beam fulfilled this condition, resulting in four SPP branches propagating in distinct directions (Supplementary Fig. S1). Two of them, traveling toward the electrode–silicon interface, contribute to the photocurrent, separated by splitting angles  $\pm\theta$  relative to the x-axis. As  $m$  increases, the in-plane component  $\mathbf{k}_{\text{OAM}}$  increases, leading to a larger  $\theta$  according to the law of cosines, as confirmed by simulation (Fig. 1c). Consequently, SPPs excited by higher-order OAM beams propagate over longer distances and undergo greater loss. These SPPs are subsequently reconverted into optical fields by the output grating at the electrode–silicon interface and then transformed into photocurrents via the photovoltaic effect at the Schottky junction. The photocurrent amplitude decreases with increasing  $m$  (Fig. 1c). By exploiting this OAM-resolved plasmonic coupling mechanism, the device discriminates vortex beams from  $|m| = 1$  to 9 with an average OAM responsivity of  $R_{\text{OAM}} = \frac{\Delta I_{\text{ph}}}{P \cdot \Delta m}$ , where  $I_{\text{ph}}$  is the photocurrent, and  $P$  is the incident power. The measured  $R_{\text{OAM}}$  reaches 226 nA W<sup>-1</sup>, surpassing all previously reported results (Fig.

1d).

To experimentally validate the OAM-resolving grating concept, we first designed and fabricated a baseline photodetector as shown in Fig. 2. The input grating period  $\Lambda$  was selected to satisfy the coupling condition as  $|\mathbf{k}_{SPP}| - |\mathbf{k}_{OAM}| < \frac{2\pi}{\Lambda} < |\mathbf{k}_{SPP}| + |\mathbf{k}_{OAM}|$ . In subsequent experiments,  $\Lambda = 610$  nm was chosen such that  $\mathbf{G} \approx \mathbf{k}_{OAM}$  at the 633 nm excitation wavelength. Under this condition, the SPP splitting angle  $\theta$  increases from zero as the incident OAM order  $m$  increases. The grating parameters were optimized through finite-difference time-domain (FDTD) simulations. Maximum coupling efficiency was achieved at a slot width of 80 nm and a depth of 120 nm (Supplementary Fig. S2). The input grating length  $l_{gra}$  was set to  $\sim 12$   $\mu\text{m}$  with 20 periods, ensuring full coverage of the vortex beam (Fig. 2c). To balance responsivity and OAM resolution, the center-to-electrode distance  $D$  was designed as 30  $\mu\text{m}$ , while the electrode width  $w_{ele}$  was set to 40  $\mu\text{m}$  to suppress edge reflection and scattering. The output grating shared the same period as the input grating and consisted of a four-period pattern along the electrode edge.

FDTD simulations of the intensity on the electrode surface under vortex illumination with  $m = +1$  to  $+9$  are shown in Fig. 2a (Supplementary Note 2). The averaged intensity profiles along the electrode edge, normalized to the peak value at  $m = 1$ , are presented in the side panel. Here, a vortex beam with clockwise rotation is defined as positive. The excited SPPs form two counter-propagating branches directed upward and downward. With increasing  $m$ , the separation between the branches widens progressively but with a diminishing rate, which is consistent with the gradual saturation of  $\mathbf{k}_{OAM}$ . It is worth noting that the angular distribution of the SPP emission spans a broad range. This arises from spatial variations in the vortex wavefront, which actually contains a continuum of  $\mathbf{k}_{OAM}$  components. The SPP splitting angle  $\theta$  was extracted along the

direction of maximum intensity, and theoretical calculations were performed using the same criterion (Supplementary Note 1). The simulated and theoretical results (Fig. 2e) show excellent agreement, confirming the OAM discrimination mechanism. As  $m$  increases, the total SPP power reaching the electrode edge decreases due to enhanced propagation loss. Additionally, the rate of this decrease diminishes at higher  $m$ , which is consistent with the expectations. Moreover, the downward-propagating branch exhibits notably higher intensity than the upward branch, attributed to their distinct excitation positions. SPPs in the upward branch are launched further from the electrode–silicon interface and experience stronger grating losses. When the chirality of the incident vortex beam is reversed, the relative intensities of the two SPP branches also invert.

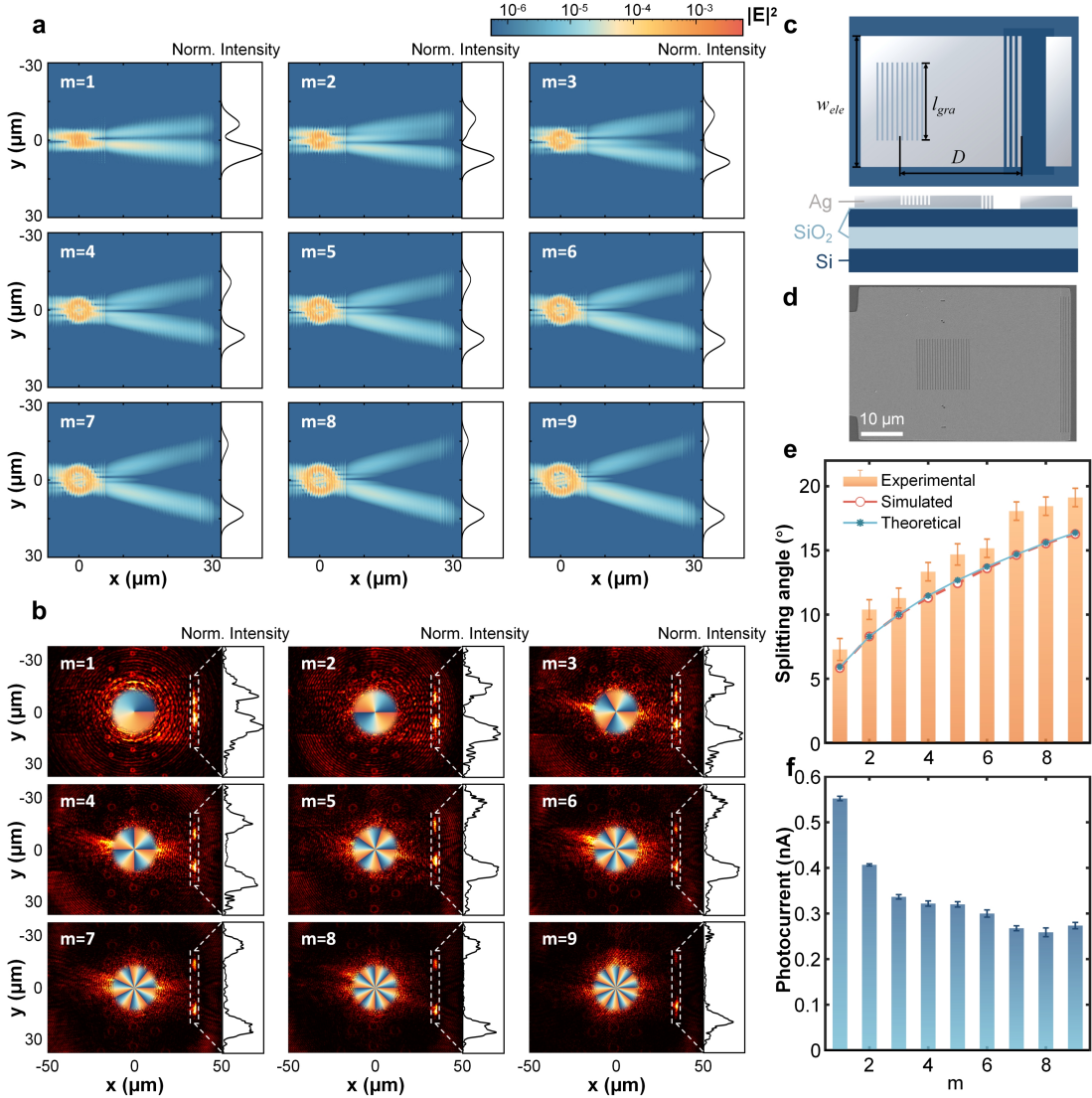


**Fig. 2 Numerical simulation and experimental characterization of the grating-based OAM photodetector.**

**a.** Simulated light intensity on the silver electrode surface under vortex beams with  $m = 1\text{-}9$ . Side panels: corresponding normalized intensity profiles along the  $y$ -axis at the output grating position. **b.** Experimentally measured intensity distributions for  $m = 1$  to 9. The contrast of the images has been additionally enhanced for visualization. The white dashed boxes denote the output coupling grating region where SPP splitting is observed. Side panels: integrated intensity profiles within the boxed regions, normalized to the peak intensity of the  $m = 1$  mode. **c.** Top-view (upper) and cross-sectional (lower) schematics of the device architecture. **d.** Scanning electron microscopy (SEM) image of a representative fabricated device. **e.** Comparison of the SPP

splitting angles obtained from theoretical calculations (blue), numerical simulations (red), and experimental measurements (orange bars) for  $m = 1-9$ . Error bars represent the average full width at half maximum of measurements. **f.** Measured photocurrent as a function of the incident OAM order  $m$ . The error bars are the standard deviation of three measurements.

Devices with the optimized parameters were fabricated on a silicon-on-insulator (SOI) substrate. A  $\text{SiO}_2$  insulating layer was first deposited, with the region between the two electrodes selectively etched to form a Schottky contact. The insulating layer prevents short-circuiting through the top silicon layer in non-active areas, and also prevents the possible excessive etching of input gratings during fabrication. The electrodes were patterned using electron-beam lithography followed by electron-beam evaporation, while the gratings were defined by focused ion beam milling (see Methods for details). To avoid spurious photocurrent generation, the input grating was designed not to penetrate the metal electrode (Supplementary Fig. S3). In contrast, the output grating was etched through the electrode to enhance optical-to-electrical conversion efficiency. An SEM image of a representative device is shown in Fig. 2d. During measurements, vortex beams were generated using a Q-plate. After being slightly focused by an objective lens, the beam was normally incident on the input grating, exciting SPPs that propagated toward the electrode-silicon interface. A portion of the SPP field was outcoupled into free space via the output grating and collected along the optical path for imaging (Supplementary Fig. S4).

The measured SPP mode distributions under incident beams with  $m = 1-9$  are presented in Fig. 2b. The side panel shows the average normalized light intensity along the  $y$ -direction at the electrode edge, corresponding to the white box in the image. The experimental results agree closely with

both theoretical and simulated predictions: as the OAM order  $m$  increases, the SPP beam splitting angle enlarges, while the edge intensity gradually decreases. Minor fluctuations at the intensity peaks are attributed to stripe noise caused by reflected light from the grating captured by the CMOS. At higher  $m$ , the splitting angle exhibits a saturation trend, consistent with theoretical expectations (Fig. 2e). The photoresponse of the device is shown in Fig. 2f. As  $m$  increases, the photocurrent gradually decreases, demonstrating direct OAM-to-electrical conversion. However, as revealed by the measurements (Fig. 2f) and the simulations (Fig. 3a), the photocurrent variation rate rapidly converges toward zero with increasing  $m$ . Consequently, for vortex beams with  $m > 4$ , the photocurrent change induced by a one-unit difference in OAM order becomes comparable to the noise level, hindering effective discrimination. Additional structural optimization is therefore required to enhance the distinction between SPP modes excited by higher-order vortices and to further expand the detectable OAM range.

### **Enhancing the detection capacity through dielectric lenses**

Depositing a dielectric film on a metal surface modifies the propagation constant of SPPs, changing their effective refractive index. Consequently, patterned dielectric layers can serve as plasmonic lenses to focus or diverge SPP waves. Their focal length follows an expression analogous to that of traditional lenses:  $\frac{1}{f} = (\Omega - 1) \left( \frac{1}{R_1} - \frac{1}{R_2} + \frac{(\Omega-1)t}{n_2 R_1 R_2} \right)$ , where  $f$  is the plasmonic focal length,  $R_1$  and  $R_2$  are the radii of curvature on both sides,  $n_1$  and  $n_2$  denote the real parts of the effective indices in regions without and with the dielectric,  $t$  is the central thickness, and  $\Omega = n_2/n_1$ . Introducing a concave plasmonic lens between the input and output gratings (Fig. 3a) enlarges the SPP splitting angle and increases the propagation-loss contrast, thereby enhancing the

discrimination of high-order OAM states (Supplementary Fig. S5). Geometrically, SPPs excited by high-order vortices also propagate longer distances inside the lens, experiencing stronger attenuation. Collectively, these effects endow the lens-integrated device with a markedly improved resolving capability when compared to the baseline design, as evidenced in the normalized transmission efficiencies shown in Fig. 3b.

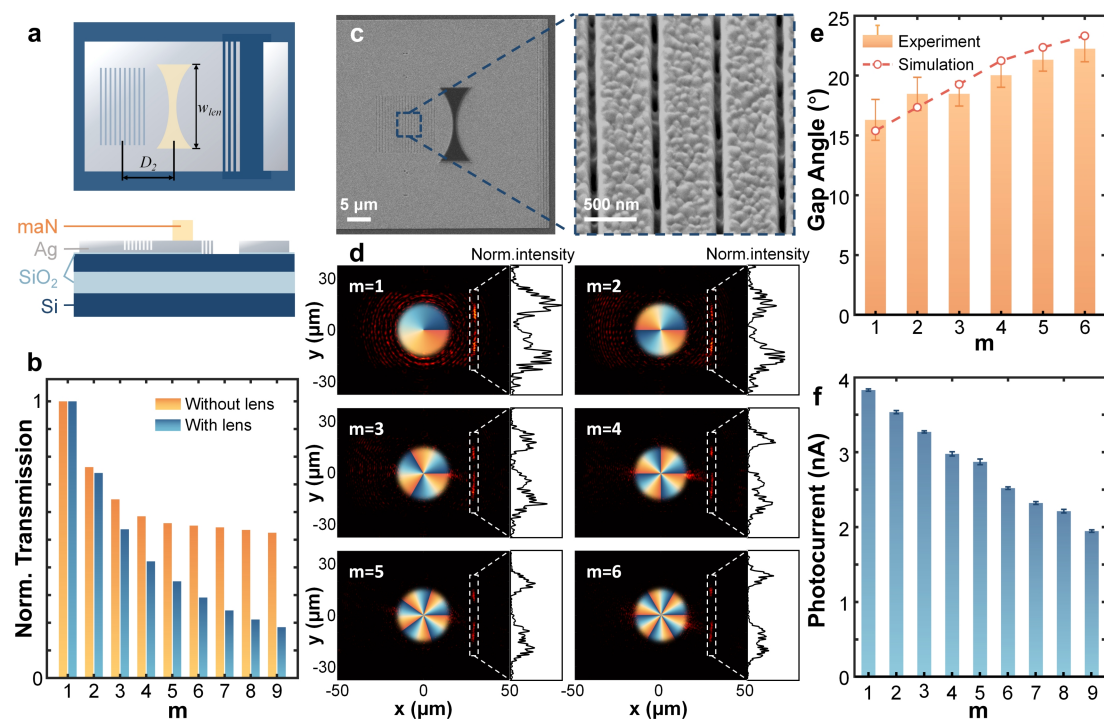


**Fig. 3 Optical and optoelectronic characterization of the lens-integrated OAM photodetector.**

**a.** Top-down (upper) and cross-sectional (lower) schematic of the photodetector incorporating a plasmonic lens **b.** Simulated normalized transmission as a function of OAM order  $m$  for devices with (blue) and without (orange) the integrated lens. **c.** SEM images of the fabricated lens-integrated device. The inset provides a magnified view of the input coupling grating structures. **d.** Measured optical intensity distributions for OAM orders  $m = 1-6$ . The contrast of the images has been enhanced for visualization. The white dashed boxes indicate the output grating

region. Side panels: corresponding normalized intensity profiles along the  $y$ -axis, showing the spatial separation of the SPPs. **e.** Simulated (red) and experimentally measured (orange) SPP splitting angles for  $m = 1\text{-}6$ . Error bars represent the average full width at half maximum. **f.** Measured photocurrent response of the optimized photodetector under vortex beam illumination for OAM orders ranging from 1 to 9. The error bars are the standard deviation of three measurements.

Experimentally, an additional electron-beam exposure step was used to pattern a concave dielectric lens made of maN photoresist, as shown in the SEM image in Fig. 3c. The optimized focal length  $f=8\text{ }\mu\text{m}$  and the center-to-grating distance  $D_2=10\text{ }\mu\text{m}$  were obtained through global FDTD optimization. Following the same optical measurement procedure, the SPP splitting angle and photocurrent of the new device were characterized. As shown in Fig. 3d and e, the SPP splitting angle increases significantly, in agreement with the simulations. Here, the splitting angle is also defined as the angle between the line connecting the output SPP lobe and the vortex-beam center and the x-axis for consistency. Due to reflection and interference at the lens interface, each SPP branch becomes broadened and exhibits multi-peak intensity features, consistent with the simulation results in Supplementary Fig. S6. The measured photocurrent (Fig. 4f) decreases steadily with increasing OAM order and follows an overall linear trend, enabling direct electrical readout of vortex beams from  $m = 1$  to  $m = 9$ . The average OAM responsivity reaches  $R_{\text{OAM}}=226\text{ nA}\cdot\text{W}^{-1}$ , significantly exceeding previously reported values. The device also exhibits an exceptionally low dark current of  $0.95\text{ pA}$ , yielding a noise-equivalent OAM resolution as low as  $\text{NE}\Delta m = I_{\text{noise}}/(dI_{\text{ph}}/dm) = 0.05\text{ Hz}^{-1/2}$  at the  $-3\text{dB}$  cut-off frequency (noise spectrum in

Supplementary Fig. S7).

Compared with commercial silicon detectors, the response speed is much slower, with rise and fall times of 605  $\mu$ s and 845  $\mu$ s, respectively (Supplementary Fig. S8), corresponding to a cutoff frequency of  $\sim$ 572 Hz. Further measurements indicate that the reduced speed is attributable to parasitic capacitance induced by the 20 nm SiO<sub>2</sub> insulating layer between the electrode pad and the SOI substrate. Removing the top-silicon layer in non-active regions not only prevents electrical shorting but also suppresses this parasitic capacitance. Based on this approach, a high-speed OAM photodetector was fabricated (Supplementary Fig. S9), achieving a rise/fall time of 1.70/1.83  $\mu$ s (Supplementary Fig. S9). As this value attends the modulation limit of the laser source used, the intrinsic device speed may be even higher. However, the responsivity of this high-speed device is substantially decreased, which limits its applicability in direct detection of high-order OAM modes (Supplementary Fig. S10). With a refined electrical design, we anticipate that both parasitic capacitance and excess noise can be effectively suppressed, enabling a high-speed, low-noise photodetector for robust vortex-beam OAM sensing.

## Chirality Discernibility in a Split-Electrode Device

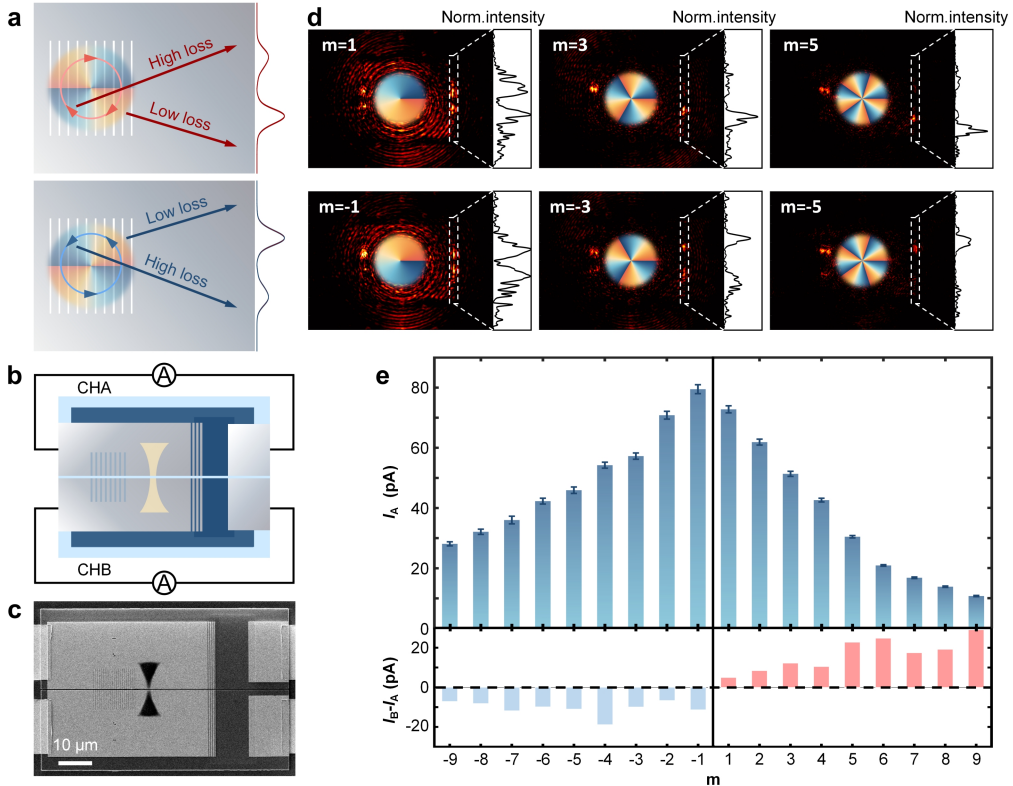


**Fig. 4 Discrimination of OAM order in a split-electrode photodetector.** **a.** Operational principle for chirality-resolved OAM detection. Asymmetric loss during SPP propagation enables the separation of vortex modes with opposite chirality. **b.** Schematic of the chirality-resolving device. **c.** SEM image of the fabricated split-electrode photodetector. **d.** Intensity distributions of the device under vortex beams with opposite chirality ( $m = \pm 1, \pm 3, \pm 5$ ). The contrast has been enhanced for visualization. The white dashed boxes indicate the output grating regions. Side panels: corresponding normalized intensity profiles along the  $y$ -axis. **e.** Optoelectronic performance of the split-electrode device. Upper panel: measured photocurrent  $I_A$  in Channel A as a function of OAM order  $m$  from -9 to +9. Lower panel: photocurrent difference ( $I_B - I_A$ ) between the two channels.

Reversing the chirality of the incident vortex beam inverts the relative intensities of the excited SPP branches while maintaining the total SPP power that reaches the Schottky junction. Consequently, the single-electrode configuration discussed above can only resolve the magnitude of the OAM order ( $|m|$ ), with the sign remaining indeterminate. To overcome this limitation, a modified device architecture was proposed to distinguish the spatial intensity asymmetry of the SPP branches, thereby enabling unambiguous chirality detection. The working principle is illustrated in Fig. 4a. For a vortex beam with positive OAM order  $+m$ , momentum matching excites two SPP branches propagating toward the electrode–silicon interface. Due to geometric asymmetry, the upward-propagating branch traverses more grating periods and suffers higher propagation loss than the downward branch. This intensity disparity, confirmed by previous simulations and experiments (Figs. 2b and 3d), inverts when the OAM chirality is reversed (Supplementary Fig. S11). Therefore, monitoring the intensity contrast between the two branches allows for chirality discrimination.

We implemented this concept using a split-electrode configuration (Fig. 4b), where the top silicon layer, Ag electrode, grating, and lens are physically bisected into two electrically isolated sections. These upper and lower halves function as independent photodetectors (Supplementary Fig. S12), connected to channels A and B of a picoammeter for simultaneous measurement ( $I_A$  and  $I_B$ ). Fig. 4c shows an SEM image of the fabricated device. To clearly visualize the SPP distribution, Fig. 4d presents the extracted intensities for a reference device without a dielectric lens. For  $+m$  inputs, the downward SPP branch is significantly more intense than the upward one, with the contrast becoming more pronounced at higher  $|m|$ . For  $-m$ , this distribution is reversed. The corresponding

photocurrent response (Fig. 4e) confirms the behavior of  $I_A > I_B$  for positive OAM and  $I_B > I_A$  for negative OAM. Simultaneously, the overall photocurrent magnitude decreases with  $|m|$ , preserving the capability to determine the OAM order. Thus, the device successfully resolves both OAM chirality and magnitude from  $m = -9$  to  $+9$ . Although our measurements were limited to  $|m| \leq 9$  by the generation limit of the Q-plate, the device is theoretically capable of resolving higher-order OAM modes, provided the photocurrent variation induced by OAM changes exceeds the system noise floor.

## Discussion

In summary, we have demonstrated a compact silicon-based photodetector that can directly convert the orbital angular momentum of light into distinct electrical signals. By encoding the OAM order of vortex beams into the splitting angle and propagation loss of SPPs, the device can reliably discriminate OAM states from  $m = -9$  to  $+9$ . The integration of a dielectric lens and a split-electrode architecture further enhances the resolution of high-order modes and enables unambiguous chirality determination. With a record-high average OAM responsivity of 226  $\text{nA} \cdot \text{W}^{-1}$ , this work represents a substantial advancement from previous on-chip schemes.

While the experimental demonstration was bounded by the generation limit of the Q-plate array, numerical analysis indicates the potential to resolve even higher OAM orders. Currently, the device operation speed is primarily constrained by parasitic capacitance and trade-offs with noise performance. Further optimization of electrode geometry and electrical layout is expected to alleviate these limitations, opening a pathway toward MHz-bandwidth operation without compromising sensitivity. Looking ahead, the scalability of this OAM detection method offers

diverse opportunities for next-generation high-capacity photonic systems. The grating coupling mechanism is inherently tunable, provided that the plasmonic material supports SPP propagation with appropriate losses. Given that silver maintains negative permittivity and low loss below its plasma frequency, our scheme can be readily adapted to telecommunication wavelengths by rescaling the geometric parameters and incorporating narrowband semiconductors. Furthermore, the direct electrical readout and full compatibility with standard semiconductor processing enable seamless integration with electronic and photonic circuits. This capability enables the device as a promising building block for applications including high-dimensional quantum key distribution<sup>27</sup>, on-chip optical neural networks<sup>28</sup>, high-capacity optical communication<sup>4</sup>, and multidimensional light information imaging<sup>29</sup>. Ultimately, this work establishes a solid foundation for exploiting the unbounded degree of light OAM in integrated photonic technologies.

## Methods

### Device Fabrication

The chirality-resolved devices (Fig. 4) were fabricated on SOI substrates with a 500-nm n-type top silicon layer. First, the split-silicon structures were defined by electron-beam lithography (EBL; ELS-F125, Elionix, Tokyo, Japan) using maN-2405 resist, followed by inductively coupled plasma (ICP) etching (PlasmaPro 100 Cobra, Oxford Instruments, Abingdon, England) down to the buried oxide. A 20-nm SiO<sub>2</sub> insulating layer was deposited via atomic layer deposition (ALD; MNT-S200Oz, MNT Micro and Nanotech, Changzhou, China). To expose the active silicon contact areas, a second EBL step (950 PMMA) and subsequent SiO<sub>2</sub> ICP etching were performed. The plasmonic excitation and propagation regions were defined by a third EBL step (950 PMMA),

followed by electron-beam evaporation of Ti/Ag (5/160 nm) and lift-off. Peripheral electrodes were patterned via a fourth EBL process, followed by magnetron sputtering of Ti/Ag (5/50 nm) and lift-off. Input and output coupling gratings were milled using a focused ion beam (FIB; Crossbeam 540, Zeiss, Jena, Germany). A 3-nm Al<sub>2</sub>O<sub>3</sub> passivation layer was deposited by ALD to prevent silver oxidation. Finally, the dielectric lenses were patterned using EBL with maN-2405 resist.

Fabrication for the lens-integrated devices (Fig. 3) followed a simplified protocol: the initial silicon etching step was omitted, and the plasmonic region and peripheral electrodes were patterned in a single EBL/evaporation step (Ti/Ag, 5/160 nm), eliminating the need for an additional EBL and sputtering. For the baseline devices (Fig. 2), the process was further streamlined by excluding the final dielectric lens patterning.

## Optoelectronic Characterization

Measurements were performed using a custom-built optoelectronic setup. A continuous-wave 633 nm HeNe laser (16194, REO, Colorado, USA) beam was directed through an optical switch and a quarter-wave plate, then converted into vortex beams with distinct OAM orders using a Q-plate array (VRA-633, LBTEK, Changsha, China). OAM orders were verified using an interferometric setup, with interference patterns recorded by a CMOS camera (Supplementary Fig. S13). The vortex retarder array was mounted on a motorized XY stage to allow rapid switching between OAM states. A linear polarizer aligned the beam polarization parallel to the grating vector for optimal coupling, and the beam was focused normally onto the input grating using an objective lens.

Photocurrents were recorded with a dual-channel picoammeter (6482, Keithley, Ohio, USA). Noise spectra and temporal responses were characterized using a lock-in amplifier (MFLI, Zurich Instruments, Zurich, Switzerland) and an oscilloscope (4262, Pico Technology, London, England), respectively. Incident power was calibrated using a power meter (PM101, Thorlabs, New Jersey, USA). SPP propagation images were captured using a CMOS camera.

## **Data availability**

All data needed to evaluate the conclusions in the paper are present in the paper and the Supplementary Materials. Further data that support the findings of this study are available from the corresponding authors upon reasonable request.

## **Acknowledgements**

This work was supported by the National Key Research and Development Program of China (Grant No. 2024YFA1209201 and 2022YFA1604304) and the National Natural Science Foundation of China (Grant No. 12574405 and 92250305). We also thank the State Key Laboratory of Regional Fiber Optic Communication Networks and Novel Optical Communication Systems for nanofabrication facility support.

## **Author Contributions**

G.Z and X.M contributed equally to this work. G.L and G.Z conceived the idea. G.Z and X.M carried out investigations and numerical simulations. G.Z, Z.C, H.L, X.M and S.H helped with the setup construction. G.Z finished the device fabrication. G.Z and X.M collaborated to complete the

measurements. And all authors listed contributed to the manuscript writing, reviewing, and editing.

## Conflict of interest

The authors declare no competing interests.

Supplementary information accompanies the manuscript on the *Light: Science & Applications* website (<http://www.nature.com/lsa>).

## References

1. Padgett, M. & Bowman, R. Tweezers with a twist. *Nature Photon* **5**, 343–348 (2011).
2. Shen, Y. *et al.* Optical vortices 30 years on: OAM manipulation from topological charge to multiple singularities. *Light Sci Appl* **8**, 90 (2019).
3. Liu, M. *et al.* Super-resolution optical microscopy using cylindrical vector beams. *Nanophotonics* **11**, 3395–3420 (2022).
4. Zhang, Z.-K. *et al.* Deep learning-enabled ultra-broadband terahertz high-dimensional photodetector. *Nat Commun* **16**, 8133 (2025).
5. Zhang, Y. *et al.* Dual-point noncoaxial rotational Doppler effect towards synthetic OAM light fields for real-time rotating axis detection. *Light: Advanced Manufacturing* **4**, 1 (2023).
6. Wang, Y., Ru, S., Wang, F., Zhang, P. & Li, F. Experimental demonstration of efficient high-dimensional quantum gates with orbital angular momentum. *Quantum Sci. Technol.* **7**, 015016 (2022).
7. Gong, L. *et al.* Optical orbital-angular-momentum-multiplexed data transmission under high

scattering. *Light Sci Appl* **8**, 27 (2019).

8. Wang, J. *et al.* Orbital angular momentum and beyond in free-space optical communications. *Nanophotonics* **11**, 645–680 (2022).

9. Liu, S., Lou, Y. & Jing, J. Orbital angular momentum multiplexed deterministic all-optical quantum teleportation. *Nat Commun* **11**, 3875 (2020).

10. Bai, Y., Lv, H., Fu, X. & Yang, Y. Vortex beam: generation and detection of orbital angular momentum [Invited]. *Chin. Opt. Lett.* **20**, 012601 (2022).

11. Hickmann, J. M., Fonseca, E. J. S., Soares, W. C. & Chávez-Cerda, S. Unveiling a Truncated Optical Lattice Associated with a Triangular Aperture Using Light's Orbital Angular Momentum. *Phys. Rev. Lett.* **105**, 053904 (2010).

12. Wen, Y. *et al.* Spiral Transformation for High-Resolution and Efficient Sorting of Optical Vortex Modes. *Phys Rev Lett* **120**, 193904 (2018).

13. Guo, Y. *et al.* Spin-decoupled metasurface for simultaneous detection of spin and orbital angular momenta via momentum transformation. *Light Sci Appl* **10**, 63 (2021).

14. He, G. *et al.* Multiplexed manipulation of orbital angular momentum and wavelength in metasurfaces based on arbitrary complex-amplitude control. *Light Sci Appl* **13**, 98 (2024).

15. Yue, Z., Ren, H., Wei, S., Lin, J. & Gu, M. Angular-momentum nanometrology in an ultrathin plasmonic topological insulator film. *Nat Commun* **9**, 4413 (2018).

16. Ren, H. *et al.* Orbital-Angular-Momentum-Controlled Hybrid Nanowire Circuit. *Nano Lett.* **21**, 6220–6227 (2021).

17. Mei, S. *et al.* On-chip discrimination of orbital angular momentum of light with plasmonic nanoslits. *Nanoscale* **8**, 2227–2233 (2016).

18. Ren, H., Li, X., Zhang, Q. & Gu, M. On-chip noninterference angular momentum multiplexing of broadband light. *Science* **352**, 805–809 (2016).
19. Feng, F., Si, G., Min, C., Yuan, X. & Somekh, M. On-chip plasmonic spin-Hall nanograting for simultaneously detecting phase and polarization singularities. *Light Sci Appl* **9**, 95 (2020).
20. Spektor, G. *et al.* Revealing the subfemtosecond dynamics of orbital angular momentum in nanoplasmonic vortices. *Science* **355**, 1187–1191 (2017).
21. Genevet, P., Lin, J., Kats, M. A. & Capasso, F. Holographic detection of the orbital angular momentum of light with plasmonic photodiodes. *Nat Commun* **3**, 1278 (2012).
22. Dai, M., Wang, C., Sun, F. & Wang, Q. J. On-chip photodetection of angular momentums of vortex structured light. *Nat Commun* **15**, 5396 (2024).
23. Ji, Z. *et al.* Photocurrent detection of the orbital angular momentum of light. *Science* **368**, 763–767 (2020).
24. Lai, J. *et al.* Direct Light Orbital Angular Momentum Detection in Mid-Infrared Based on the Type-II Weyl Semimetal TaIrTe<sub>4</sub>. *Advanced Materials* **34**, 2201229 (2022).
25. Yang, D. *et al.* Dimensionality-enhanced mid-infrared light vortex detection based on multilayer graphene. *Light Sci Appl* **14**, 116 (2025).
26. Yang, D. *et al.* High-speed readout for direct light orbital angular momentum photodetector via photoelastic modulation. *Adv. Photon.* **7**, (2025).
27. Huang, J. *et al.* Integrated optical entangled quantum vortex emitters. *Nat. Photon.* **19**, 471–478 (2025).
28. Guo, H. *et al.* Optical-Vortex-Convolution-Enhanced Neural Network. *Laser & Photonics Reviews* **19**, e00927 (2025).

29. Neshev, D. N. & Miroshnichenko, A. E. Enabling smart vision with metasurfaces. *Nat. Photon.* **17**, 26–35 (2023).